ACS NANO

www.acsnano.org

Human-Body-Temperature Triggerable Phase Transition of W-VO_2@PEG Nanoprobes with Strong and Switchable NIR-II Absorption for Deep and Contrast-Enhanced Photoacoustic Imaging

Liantong Li, Huazhen Chen, Yujiao Shi,* and Da Xing*

Cite This: *ACS Nano* 2022, 16, 2066−2076

Read Online

ACCESS | Metrics & More | Article Recommendations | Supporting Information

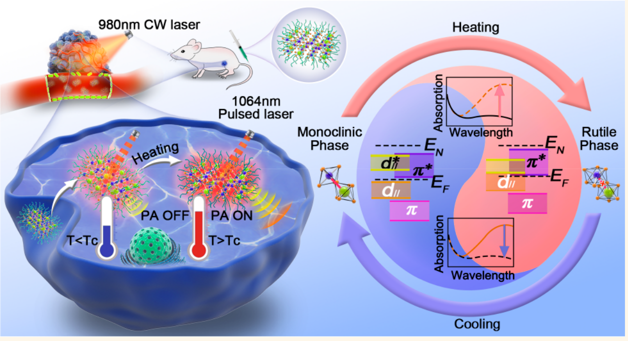

ABSTRACT: The immense potential of temperature-responsive nanomaterials for use as contrast agents has propelled much recent research and development in the field of photoacoustic (PA) imaging, while the exorbitant transition temperature exceeding the human-tolerable range and the low reversibility of the reported temperature-sensitive nanosystems are still two severe issues that hinder effective imaging and long-term monitoring in practical applications. Herein, we propose a high-performing thermoresponsive polyethylene glycol-coated tungsten-doped vanadium dioxide (W-VO_2@PEG) nanoprobe (NP) with strong and switchable optical absorption in the near-infrared-II (NIR-II) biowindow (1000−1700 nm) near human-body temperature, to achieve deep and contrast-enhanced PA imaging. Our study shows that the PA signal amplitude of W-VO_2@PEG NPs at 1064 nm increases up to 260% when the temperature increases from 35 °C to 45 °C, with a signal fluctuation of less than 10% after 10 temperature cycles, therefore enabling great potential of "off-to-on" dynamic contrast-enhanced imaging capability in deep-seated tissues. Experiments on tissue-mimicking phantoms and *in vitro* chicken breast showed that, by levering the prepared W-VO_2@PEG NPs and dynamically modulating the temperature field with an external NIR optical stimulus, contrast-enhanced PA images of the target can be obtained with an imaging depth up to 1.5 cm. Furthermore, *in vivo* potential of the prepared thermoresponsive NPs for the detection and identification of deep-seated tumors by directly comparing to conventional "always on" NPs has been demonstrated. Our work will offer feasible guidance for the development of smart temperature-activatable PA NPs with improved imaging depth and imaging contrast.

KEYWORDS: *human-body temperature, dynamic contrast enhanced, phase transition, NIR-II, photoacoustic imaging*

As a promising biomedical imaging technology, photoacoustic (PA) imaging can combine the great spatial resolution of ultrasound (US) imaging with the excellent contrast of optical imaging through the absorption and conversion of photons to acoustic waves.[1−5] To fully realize the capabilities of the PA technique for deep-tissue functional imaging, exogenous PA imaging contrast agents have been introduced by initiatively or passively targeting the region of interest (ROI).[6−15] Compared with the conventional "always on" PA nanoprobes (NPs) that provide stable imaging contrast,[16] those activatable NPs that can provide dynamic images when under cell internal (*i.e.*, pH,[17−19] redox,[20] concentration of specific biomolecules[21]) or external (temperature field,[22] US field,[23] light of various wavelengths[24]) stimuli have shown superior imaging capability with improved contrast and sensitivity.[25−27] Among these NPs, temperature-responsive PA NPs have exhibited outstanding performance in various

Received: August 28, 2021
Accepted: January 24, 2022
Published: January 27, 2022

Scheme 1. (A) Preparation of temperature-responsive W-VO_2@PEG NPs. (B) Schematic illustration of dynamic-enhanced NIR PA imaging using W-VO_2@PEG NPs triggered by near-human-body temperature. First, W-VO_2@PEG NPs are accumulated in tumor cells. Next, the temperature of the tumor is elevated to more than 38 °C by laser irradiation, causing the phase transformation of W-VO_2@PEG NPs. Meanwhile, the NIR absorption of W-VO_2@PEG NPs increases sharply accompanied by the phase transformation, and PA signals will become stronger. Furthermore, the absorption of W-VO_2@PEG NPs can be adjust by the laser irradiation time. As a result, it is easy to realize dynamic-enhanced NIR PA imaging.

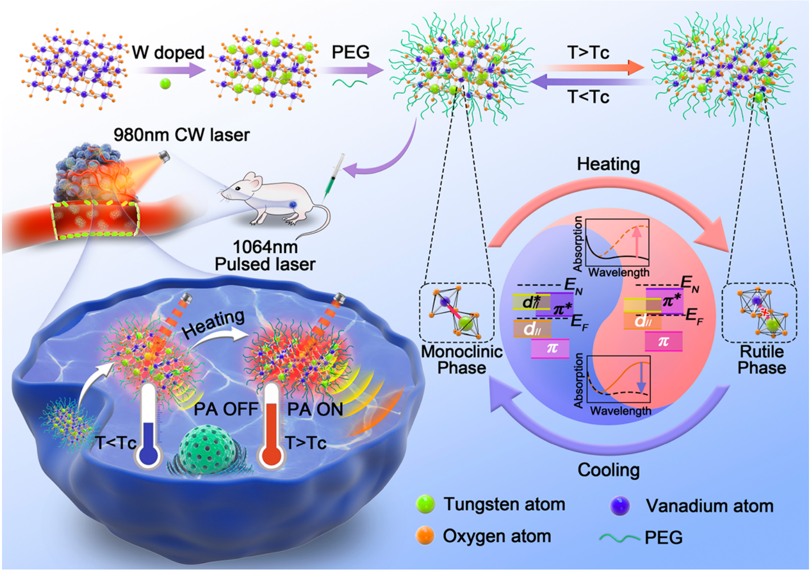

imaging applications, where the abnormal temperature changes in tissues are closely related to the occurrence and development of diseases such as cancer and inflammation.[28] However, most of the reported temperature-responsive PA NPs have faced critical issues in practical applications because the transition temperature is generally much higher than human-body temperature, and thus the potential risk of tissue thermal damage exists.[29] Moreover, these temperature-responsive NPs always rely on the irreversible release of optical nanoabsorbers by thermally triggered nanocarriers, which only provides a "one-off" thermal stimuli−response action and cannot provide long-term dynamic monitoring.[30] On the contrary, the reversible-type NPs can dynamically respond to temperature field stimulation, and thus the targeted ROI can be specifically identified with improved imaging contrast and background signal being effectively suppressed.[31,32] Polymers and lipids have been developed to build PA thermoresponsive NPs by changing the assembling or aggregation status of the nanosystems after stimuli; however, these NPs generally showed slow response speed and poor temperature sensitivity with limited dynamic range.[22,33] More alarmingly, they often show conformational lability due to the low mechanical strength and fragile nature after several repetitive stimulations and, therefore, cannot satisfy the need of long-term monitoring.[34,35] Hence, considering the reliability of the thermoresponsive NPs, it is of urgency and significance to explore agents with high sensitivity and outstanding reversible repeatability for advancing deep and contrast-enhanced PA imaging.

Herein, we report a high-performing reversible temperature-responsive polyethylene glycol (PEG)-coated tungsten-doped vanadium dioxide (W-VO_2@PEG) NP with strong and switchable near-infrared II (NIR-II, 1000−1700 nm)[36,37] PA contrast at the near-human-body temperature to realize deep and contrast-enhanced PA imaging. The developed W-VO_2@PEG NPs exhibit a typical insulator-to-metal phase transition with sharply enhanced optical absorption in the NIR-II region when exceeding their critical temperature (41.1 °C) and return back rapidly to their insulator phase (~2 μs)[38] with low absorption when the temperature drops to normal status, thus providing a sensitive "off" to "on" imaging strategy under the aid of an external near-infrared optical stimulus. Compared with NIR-I (700−950 nm) PA contrast agents, the prepared NIR-II NPs allow a much larger maximum permissible laser exposure with reduced light scattering of the tissues, which benefits contrast-enhanced PA imaging of deep-seated diseases.[39,40] The temperature-responsive ability of the as-prepared NPs was investigated under different temperatures, and the high reversibility of the material was tested in multiple temperature cycles. Then, their capabilities of depth imaging were evaluated in experiments on tissue-mimicking phantoms and *in vitro* chicken breast. Finally, we demonstrate that W-VO_2@PEG NPs can highly improve the PA imaging contrast and imaging depth in tumor detection through dynamically responding to temperature.

RESULTS AND DISCUSSION

Construction of the Thermoresponsive Contrast Agents. Vanadium dioxide (VO_2) is one of the most typical thermochromic materials that exhibit enhanced optical absorption at the high-temperature region.[41−43] Benefiting from its temperature-responsive physical properties, it has been widely explored in electronic devices and optical switches, especially for thermochromic smart windows.[44] However, VO_2 NPs are not suitable for directly applying to the biological field owing to their relatively high phase transition temperature point (T_C, about 68 °C) and poor biocompatibility.[45] Herein, in order to enable their ability for high-performance bioapplications, an ingenious tungsten (W)-doping strategy with a doping concentration of about 4% is first introduced to the VO_2 NPs to reduce their T_C to the near-human-body

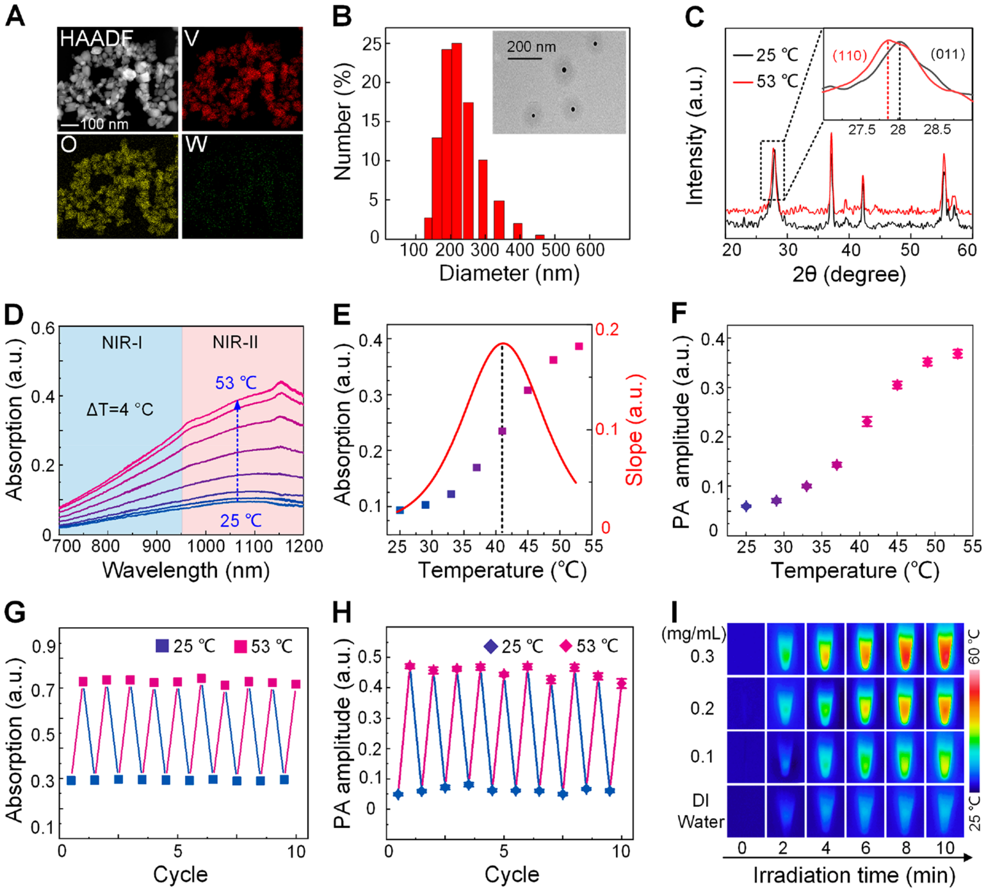

Figure 1. Characterization of the W-VO$_2$@PEG NPs. (A) Transmission electron microscope (TEM) mapping of the W-VO$_2$@PEG NPs. (B) Representative size distribution image and TEM image of W-VO$_2$@PEG NPs after being modified by PEG. (C) XRD pattern images of W-VO$_2$@PEG NPs at different temperatures. (D) UV–vis–NIR spectra of W-VO$_2$@PEG NPs at different temperatures. (E) Absorptions of W-VO$_2$@PEG NPs at different temperatures. (F) PA intensity of W-VO$_2$@PEG NPs at different temperatures. (G) Reversibility in absorption at 1064 nm during heating cycles above and below W-VO$_2$@PEG NPs' phase transition midpoint. (H) Reversibility in PA signal at 1064 nm during heating cycles above and below W-VO$_2$@PEG NPs' phase transition midpoint. (I) Temperature increase images of W-VO$_2$@PEG NPs of different concentrations at different time points.

temperature, as shown in Scheme 1. According to the reported theoretical calculations,[46] the evaluated substitution energies of W-doping in VO$_2$ for both the monoclinic insulator phase and the rutile metal phase are negative, strongly indicating that W atoms can be easily doped into a VO$_2$ lattice. Interestingly, W-doping not only reduces the T_C of VO$_2$ but also brings more free electrons to further enhance their NIR absorption (the absorption spectra before and after W-doping are shown in the Supporting Information).[47,48] Then, the W-VO$_2$ NPs are wrapped by PEG to enhance the water dispersion and to make them uniformly dispersed. When the temperature is below T_C, the W-VO$_2$@PEG NPs are in their monoclinic phase, in which two varying length V–V bonds are formed, and the $d_{\parallel}$ band is split into two energy bands ($d_{\parallel}$ and $d_{\parallel}^*$ bands), where a forbidden band with a bandwidth of about 0.7 eV is formed between the $d_{\parallel}$ and π^* bands. In this status, the Fermi level falls within the forbidden band, which makes VO$_2$ NPs permit high NIR transmission with low optical absorption. After heated up to and higher than T_C, the low-symmetry structure of the V–V bonds in VO$_2$ NPs turns to their rutile phase with a monoclinic and highly symmetrical quadrilateral structure, where the V^{4+} ions occupy the body center and the vertex of the tetragonal structure, and each V^{4+} ion and six surrounding O^{2-} ions constitute an octahedral VO$_6$ unit. In this status, the Fermi level falls between the π^* and the $d_{\parallel}$ bands, which induces a dramatic increase of the NIR-II absorption.[49−52] When W is doped into VO$_2$, the biaxial strain on the sublattices around W sites leads to the breaking of bonds between Peierls-paired V ions and lowers the transition temperature.[53,54] Given this heat-induced change in the NPs' optical absorbance, the utility of W-VO$_2$@PEG NPs as a temperature switch for dynamic-enhanced PA imaging was investigated, which therefore benefits the application of W-VO$_2$@PEG NPs in biological fields.

Characterization of the W-VO$_2$@PEG NPs. In order to characterize the element distribution in the prepared W-VO$_2$@PEG NPs, transmission electron microscope (TEM) mapping is first performed. As shown in Figure 1A, TEM mapping results confirmed localized V and O atoms in the filled core area and W atoms evenly distributed in the whole NPs. The shape of the NPs was also characterized by TEM, indicating that the W-VO$_2$ NPs had a spherical shape with an average diameter of 30 nm and are successfully modified by PEG with a total diameter of about 200 nm. The TEM image was consistent with the measurement by a particle size analyzer, where an average diameter of 200 nm was observed (Figure 1B). The crystal structures of the W-VO$_2$@PEG NPs as-prepared samples were characterized by X-ray diffraction

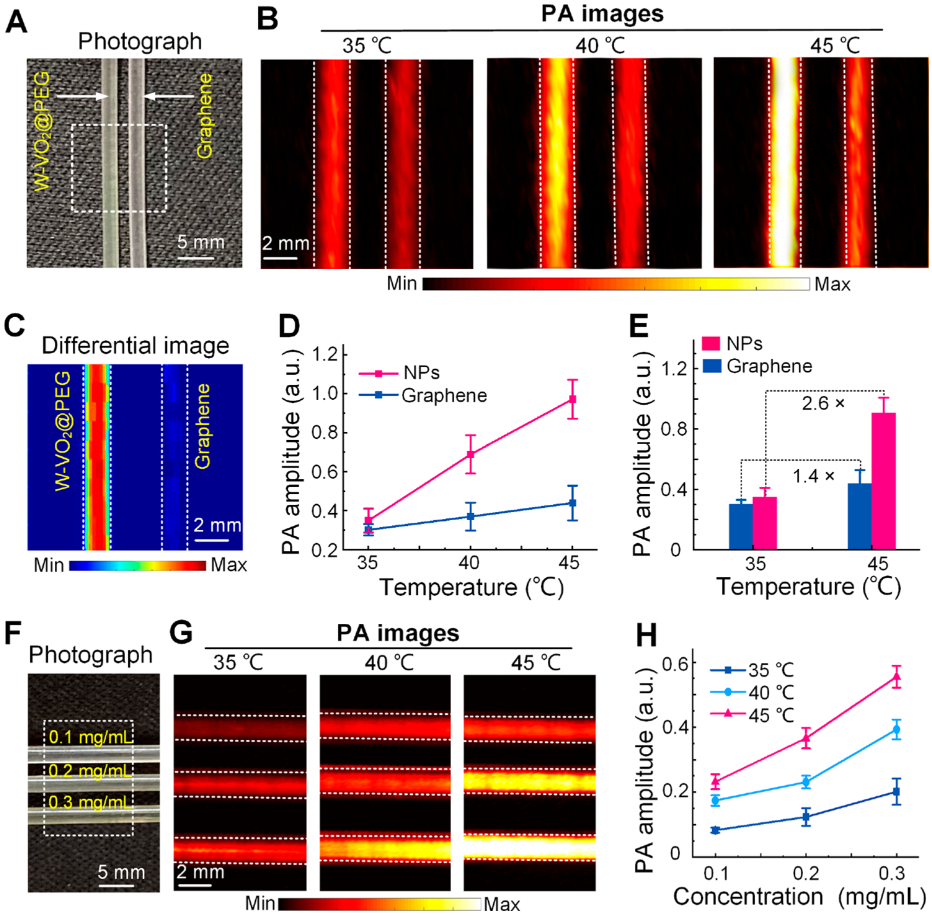

Figure 2. Temperature-responsive behavior of W-VO$_2$@PEG NPs. (A) Photograph of thin-wall polyethylene tubes filled with W-VO$_2$@PEG NPs and graphene solutions. (B) PA imaging of W-VO$_2$@PEG NPs and graphene samples at different temperatures. (C) PA difference image of W-VO$_2$@PEG NPs and graphene samples when the temperature is 45 and 35 °C. (D) Amplitude of the PA signal of B. (E) Amplitude of the PA signal of W-VO$_2$@PEG NPs and graphene samples at 45 and 35 °C. (F) Photograph and PA imaging of thin-wall polyethylene tubes filled with W-VO$_2$@PEG NPs with different concentrations at different temperatures. (G) PA imaging of W-VO$_2$@PEG NPs of different concentrations at different temperatures. (H) Amplitude of the PA signal of G.

(XRD) at 25 and 53 °C and are shown in Figure 1C. At 25 °C, only XRD peaks corresponding to the signal of the monoclinic VO$_2$ phase were observed, and all the positions of peaks were concordant with the standard reference data (JCPDS No. 82-0661), indicating the exclusive formation of single-phase VO$_2$ NPs. The results demonstrate the structural transition of the W-VO$_2$@PEG NPs from monoclinic (25 °C) to tetragonal rutile (53 °C) phase. The partially enlarged view in Figure 1C clearly shows an XRD peak shift of VO$_2$(M) (011) to VO$_2$(R) (110) peak in the $26° \leq 2\theta \leq 30°$ range when the temperature increases from low to high.[55] Furthermore, the thermochromic property of the W-VO$_2$@PEG NPs was characterized by UV−vis−NIR spectroscopy. As shown in Figure 1D, the W-VO$_2$@PEG NPs exhibited a continuous absorption from visible light to NIR region without sharp peaks when under 25 °C. After heating to near-human-body temperature, an obvious optical absorption increase in the NIR-II region was observed, which indicates the occurrence of a phase transition of the prepared W-VO$_2$@PEG NPs from monoclinic phase to rutile phase. The optical absorbance of W-VO$_2$@PEG NPs at 1064 nm as a function of temperature was then statistically analyzed in Figure 1E, and the derivative of the fitted absorption curve with temperature is also presented. It shows that the optical absorbance of the W-VO$_2$@PEG NPs greatly increases with the temperature between 35 and 53 °C, and the derivative curve indicates the largest absorption changes around 41.1 °C, which can be considered as the phase transition temperature. A similar phenomenon is observed for the PA signal amplitude (Figure 1F), which benefits the application of the W-VO$_2$@PEG NPs in temperature-triggered PA imaging. The statistical results in Figure 1F are obtained from three groups of W-VO$_2$@PEG NPs. Further, in order to demonstrate the reversibility of the phase transition for the prepared NPs, the absorption changes at 1064 nm of W-VO$_2$@PEG NPs during 10 successive heating−cooling cycles (from 25 to 53 °C) are measured, where periodic absorption changes are observed with sustainable repeatability, showing the robustness of the system (Figure 1G). Repeated heating−cooling cycles also resulted in similar periodic changes in PA signal intensity, shown in Figure 1H. Taken together, these data suggest that the phase transition is highly reversible and can be repeated over 10 heating−cooling cycles with a PA amplitude fluctuation of less than 10%. To characterize the photothermal conversion capability of the W-VO$_2$@PEG NPs, the photothermal properties of W-VO$_2$@PEG NPs with different concentrations are characterized under the irradiation of a 980 nm continuous laser (0.5 W/cm^2). As a control, a negligible temperature increase was observed for the water with irradiation at the same laser intensity. The corresponding thermal images of the W-VO$_2$@PEG NPs with different

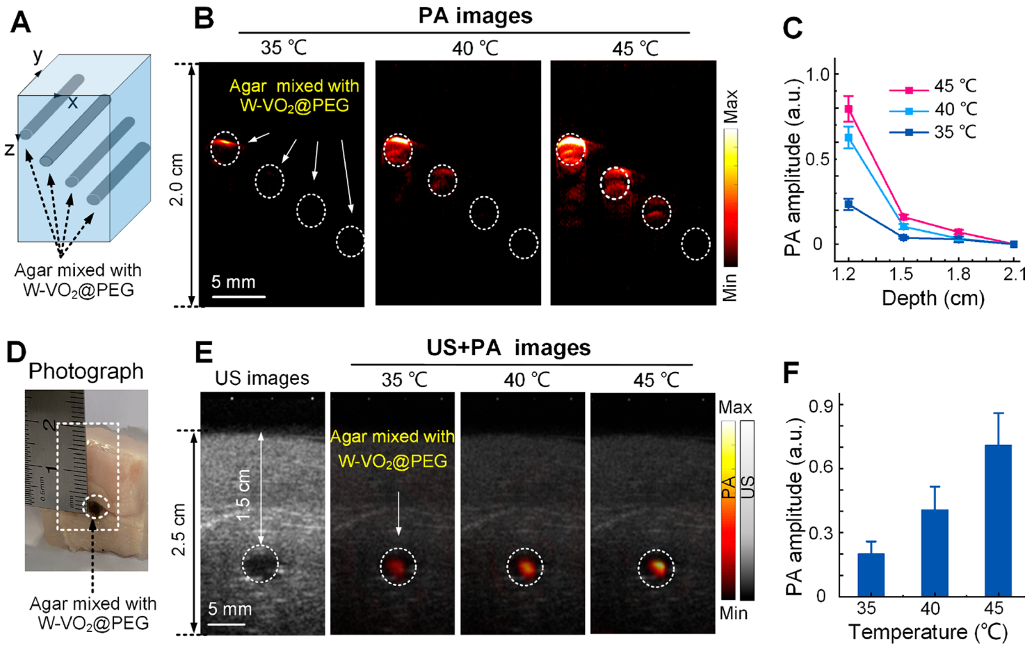

Figure 3. Verification of the deep imaging ability of W-VO_2@PEG NPs. (A) Schematic diagram of deep-tissue PA imaging of W-VO_2@PEG NPs in the agar mimic. The dotted circles indicate the positions of the samples embedded in the tissue-mimicking agar phantoms. (B) X−Z tomographic imaging at different temperatures of A. (C) Amplitude of the PA signal of B. (D) Photograph of the chicken breast sample. (E) US+PA images of X−Z tomographic imaging of D at different temperatures. The dotted circle indicates the sample's position embedded in the chicken breast tissue. (F) PA signal amplitude of E.

concentrations under different irradiation times are shown in Figure 1I. The photothermal conversion efficiency of the NPs is calculated to be ~36.7% (see the Supporting Information). All the results show that the W-VO_2@PEG NP solution can well respond to an external laser stimulus with a relatively low concentration.

PA Characterization Using Phantoms. To demonstrate the temperature-triggered PA effect of the W-VO_2@PEG NPs, a group of PA experiments were performed compared with the nonresponsive graphene solution. A sample photograph is shown in Figure 2A, and the white dotted frame indicates the imaging area. The concentration of the two samples is set to 0.2 mg/mL. During the experiments, the samples were immersed in a temperature-controlled circulating water bath with a temperature accuracy of about 0.5 °C. The excitation wavelength is 1064 nm, and the laser energy density is set to 30 mJ/cm^2. The obtained PA images under 35, 40, and 45 °C are presented in Figure 2B. The temperature range (35 to 45 °C) can basically cover all temperatures involved in the potential biological applications of the W-VO_2@PEG NPs in further studies, including PA/PT imaging, diagnosis, and therapy. The results show that the intensity of the PA images for W-VO_2@PEG NPs grows with the temperature, while for the graphene the image intensity stays almost unchanged, where the slight increase of the intensity is contributed by the positive correlation of the Grüneisen parameter with PA signal amplitude. Figure 2C is the differential image of 45 and 35 °C of Figure 2B, where the W-VO_2@PEG NP sample is clearly identified with the graphene. Therefore, when the W-VO_2@PEG NPs are positively or passively targeted to the ROI, the ROI can be specifically identified through image differential processing at different temperatures with the background signal effectively suppressed. Figure 2D shows the dependence of the PA amplitude on the temperature obtained by statistical average of the PA signal amplitudes of the samples for all imaged points corresponding to Figure 2B. As shown in Figure 2E, when the samples are heated to 45 °C, the PA signal amplitude is amplified 260% for the W-VO_2@PEG NPs, while the graphene shows a mild increase. Next, in order to show the linear dependence of the PA signal amplitude on the W-VO_2@PEG NP concentration at different temperatures, a group of W-VO_2@PEG NP samples with different concentrations are designed and imaged. The sample photograph is shown in Figure 2F, and the images at different temperature are shown in Figure 2G. With the concentration increases, the PA image becomes brighter. Figure 2H is the statistical results of the PA signal amplitude in Figure 2G, where a linear dependence of the amplitude on the concentration is observed. These results demonstrate that the prepared W-VO_2@PEG NPs show excellent potential for near-human-body-temperature-triggered high-contrast PA imaging with the background signal effectively suppressed.

Characterization of the PA Imaging Depth by Using W-VO_2@PEG NPs. One of the great advantages of the PA technique for bioimaging is its 3D imaging capability in deep-seated tissues. In this work, the prepared W-VO_2@PEG NPs exhibit strong and switchable optical absorption in the NIR-II region triggered by a near-human-body-temperature thermal field, which therefore can support their applications in deep imaging. To investigate the deep imaging capability of the W-VO_2@PEG NPs, a group of phantom experiments were performed. Figure 3A is a sketch map of the prepared phantom sample, where four tubes filled with W-VO_2@PEG NP solution are embedded in an agar phantom with different depths. The concentration of the W-VO_2@PEG NPs is 0.2 mg/mL, and the agar phantom is composed of 1.3% agar and 0.5% fat to mimic the optical scattering of biological tissue. Then, the sample was immersed in a circulating water bath with the temperature set to 35, 40, and 45 °C, respectively. In the experiments, the laser energy density is set to be 60 mJ/cm^2. After that, B-scan PA

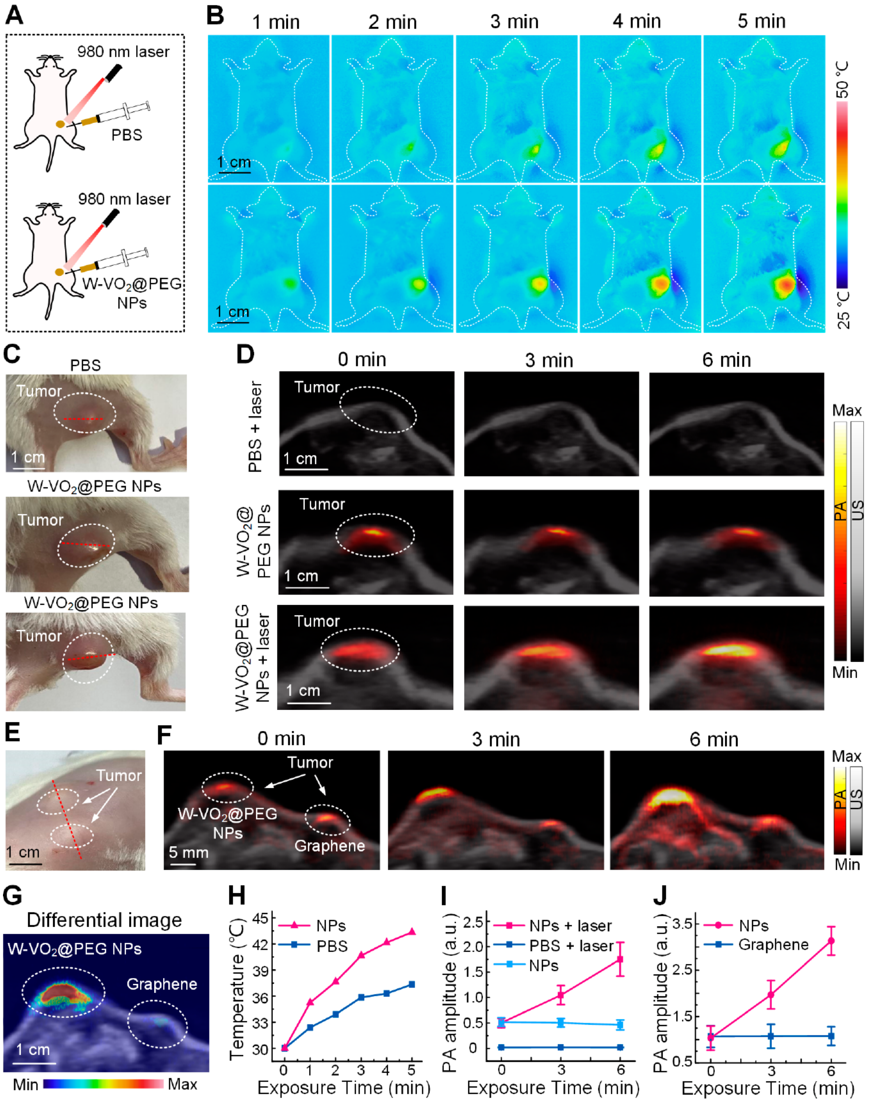

Figure 4. ***In vivo*** **PA imaging verification of W-VO$_2$@PEG NPs. (A) Schematic diagram showing temperature variation on the surface of tumors in mice under laser irradiation of 1064 nm of tumors with W-VO$_2$@PEG NPs. (B) Temperature variation on the surface of tumors in mice under laser irradiation of 1064 nm after injection with a PBS or W-VO$_2$@PEG solution. (C) Photograph of mice with tumors. The dotted circles indicate the tumor positions. (D) PA imaging of tumors at different exposure times after injection of PBS, W-VO$_2$@PEG NPs (980 nm laser off), and W-VO$_2$@PEG NPs (980 nm laser on). (E) Photograph of two tumors in a mouse. (F) PA imaging of tumors at different exposure times after injection of a graphene dispersion and W-VO$_2$@PEG NPs. (G) PA difference image + US imaging of tumors with a 6 min exposure and no exposure. (H) Temperature of tumors at different exposure times after injection of PBS and W-VO$_2$@PEG NPs. (I) PA amplitude at different exposure times after injection of PBS, W-VO$_2$@PEG NPs (980 nm laser off), and W-VO$_2$@PEG NPs (980 nm laser on). (J) PA amplitude at different exposure times after injection of W-VO$_2$@PEG NPs and a graphene dispersion.**

imaging was performed on the samples at the three temperatures. The dotted circles in Figure 3A and B indicate the positions of the samples embedded in the tissue-mimic agar phantoms. The results shown in Figure 3B indicate that the PA signal intensity increases with the temperature owing to the strong and switchable NIR-II absorption of the W-VO$_2$@PEG NPs, but decreases with the imaging depth owing to optical scattering. Figure 3C shows the statistical average of the PA signal amplitudes of the samples for all imaged points corresponding to Figure 3B. The maximum imaging depth under the three temperatures are 1.2, 1.5, and 1.8 cm, respectively. Further, to investigate the *in vitro* imaging capacity of the W-VO$_2$@PEG NPs, a tumor-mimic sample mixed with the NPs was embedded in a 1.5 cm chicken breast and imaged by the PA system. The tumor-mimic sample is a mixture of agar and W-VO$_2$@PEG NPs, and its photo is shown in Figure 3D. The white dotted box indicates the imaging region, and corresponding PA images merged with US images under different temperatures are shown in Figure 3E. The results of the PA and US image both indicate the structural information of the tumor-mimicking sample at a depth of 1.5 cm with a better image contrast for the PA image, and the PA amplitude of the tumor-mimic sample at different temperatures is shown in Figure 3F. The PA amplification ratio for Figure 3F is estimated to be 300 ± 41%, with a reasonable fluctuation to the *in vitro* result that arises from the unavoidable background signal of the chicken breast tissue.

***In Vivo* Dynamic Contrast-Enhanced PA Imaging.** To further demonstrate the thermal response of the prepared W-VO$_2$@PEG NPs, a group of *in vivo* photothermal experiments

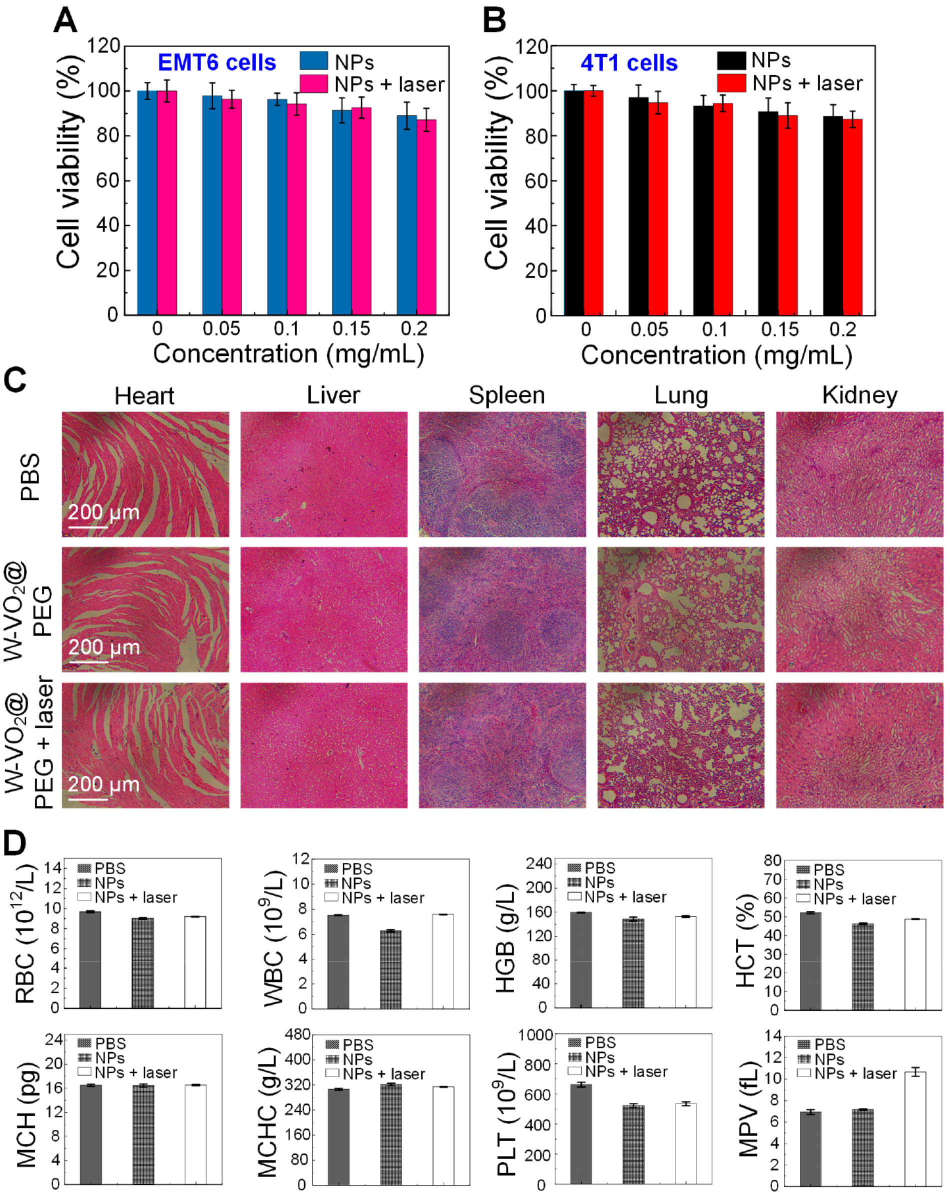

Figure 5. *In vitro* cytotoxicity assay of W-VO_2@PEG NPs. Relative viabilities of EMT6 (A) and 4T1 (B) cells after being incubated with W-VO_2@PEG NPs of varied concentrations (0.05, 0.1, 0.15, and 0.2 mg/mL). (C) H&E-stained images of different organs of mice injected with PBS, W-VO_2@PEG NPs (1.5 mg/kg, 980 nm laser off), and W-VO_2@PEG NPs (1.5 mg/kg, 980 nm laser on). (D) Blood hematology analyses of healthy nude mice after intravenous injection with PBS, W-VO_2@PEG NPs (1.5 mg/kg, 980 nm laser off), and W-VO_2@PEG NPs (1.5 mg/kg, 980 nm laser on).

were designed, as shown in Figure 4. Two mice bearing EMT6 tumors were intratumorally injected with a W-VO_2@PEG NP solution (1.5 mg/kg) and PBS (0.1 mL), where a 980 nm continuous laser (0.5 W/cm^2) was applied to elevate the temperature of tumors, as illustrated in Figure 4A. The thermal images of the tumors with different exposure times were recorded for each minute and are presented in Figure 4B. It is shown that the tumor temperature grows rapidly with the exposure time and is eventually maintained at about 43 °C for the W-VO_2@PEG NP group, where a mild temperature increase is observed for the PBS group. The average temperature increase of the tumor area with the exposure time is statistically analyzed in Figure 4H. These results indicate that the tumor area can be heated to near-human-body temperature to guarantee the phase transition of W-VO_2@PEG NPs from metallic phase to rutile phase within 5 min. Further, the two groups of tumor mice were imaged by the PA imaging system. In the experiments, the laser energy density is set to 60 mJ/cm^2. Figure 4C shows photos of the mice bearing tumors injected with PBS and W-VO_2@PEG NPs. The obtained B-scan PA images of the tumors injected with W-VO_2@PEG NPs and PBS are presented in Figure 4D. The results indicate that, compared with the PBS group, the tumor areas injected with W-VO_2@PEG NPs obviously show enhanced PA performance owing to the optical absorption in the NIR-II region of the NPs, and before the 980 nm continuous heating laser is applied (980 nm laser off), no obvious changes of the PA signal intensity with time are observed for the two groups, while for the group in which the tumor is injected with W-VO_2@PEG NPs, when exposed to a 980 nm heating laser, the W-VO_2@PEG NPs show temperature-triggered strongly enhanced PA amplitude in the NIR-II region. The average PA signal amplitude as a function of the exposure time for the three groups in Figure 4D is statistically analyzed in Figure 4I. In order to further verify the dynamic enhancement capabilities of W-VO_2@PEG NPs, we injected a graphene dispersion and W-VO_2@PEG NP solution into two tumors of the same mouse (the two tumors of the mouse are shown in Figure 4E). Then a 980 nm continuous laser (0.5 W/cm^2) was applied to elevate the temperature of the two tumors at the same time. A B-scan was performed along the red dotted line shown in Figure 4E, and the PA images are presented in Figure 4F. The obtained differential PA image is presented in Figure 4G. The statistical analysis of the PA amplitude with irradiation time for the two tumors injected with the NPs and PBS is presented in Figure 4J. The differential image of unexposed image and exposed image of 6 min are shown in Figure 4G. It is indicated that for the group in which the tumor is injected with W-VO_2@PEG NPs, when exposed to a 980 nm continuous laser, the W-VO_2@PEG NPs show a strong temperature-triggered enhanced PA amplitude in the NIR-II region. Benefiting from the temperature-triggered enhanced PA performance of the W-VO_2@PEG NPs, the tumor area can be specifically identified with suppressed background signal by a differential process of PA images under different exposure times. These results indicate that W-VO_2@PEG NPs have great potential for PA imaging enhanced through dynamic contrast enhancement.

***In Vivo* Toxicity Evaluation.** Here, we investigated the cytotoxicity of W-VO_2@PEG NPs with a CCK-8 assay. Figure 5A and B are statistically analyzed by three groups of EMT6 (A) and 4T1 (B) cells after being incubated with W-VO_2@PEG NPs. As shown in Figure 5A and B, W-VO_2@PEG NPs caused no significant EMT6 and 4T1 cell cytotoxicity, as the relative viability was higher than 85% even with treatment at 200 μg/mL. Meanwhile, we evaluated the pathological structure of main organs of mice injected with NPs. After 24 h of intravenous injection of PBS, W-VO_2@PEG NPs (1.5 mg/kg, 980 nm laser off), and W-VO_2@PEG NPs (1.5 mg/kg, 980 nm laser on) the main organs were harvested, fixed in 10% buffered formalin, processed routinely into paraffin, cut into sections, stained with H&E, and examined by optical microscopy. As seen in Figure 5C, no apparent organ damage can be observed from all the groups. Moreover, the mice were divided into three groups (n = 4) to intravenously inject with PBS, W-VO_2@PEG NPs (1.5 mg/kg, 980 nm laser off), and W-VO_2@PEG NPs (1.5 mg/kg, 980 nm laser on). After 24 h, the serum biochemical and hematological parameters for the three groups were investigated systematically. The results in Figure 5D show that, compared with the PBS group, no obvious abnormal changes were observed for the tested groups, indicating that the prepared NPs did not cause obvious infection or inflammation in the mouse model. The characteristics of W-VO_2@PEG NPs including low cytotoxicity, great photothermal stability, and strong penetration capability in tissue make them promising photothermal agents for application in the NIR-II window.

There are two distinct advantages of the temperature responsibility of W-VO_2@PEG NPs in PA imaging. First, benefiting from the strong and switchable temperature-sensitive optical absorption of the NPs in the NIR-II region, the PA imaging contrast can be dynamically enhanced, which is conducive to obtaining high-performing PA images in deep tissues. Second, different from morphologically altering-type temperature-responsive NPs, the phase transition of W-VO_2@PEG NPs occurs at the lattice level with no obvious morphological changes, thus effectively avoiding metabolic changes of the NPs arising from phase transition. Given these features, the W-VO_2@PEG NPs are significantly advantageous applied to cancer or brain molecular imaging to meet the requirements of contrast-enhanced and deep-tissue imaging with guaranteed probe metabolism. Theoretically, with W-doping concentration increases, the PA signal amplitude will become larger.[56] However, as the phase transition temperature of the W-VO_2 NPs is also determined by the W-doping concentration, further increasing the doping concentration will reduce the phase transition temperature to a lower temperature that can no longer satisfy relevant biological applications. Furthermore, benefiting from the deep-tissue-penetration ability of the external NIR optical stimulus located at the bio-optical window, the W-VO_2@PEG NPs accumulated at the region of interest can be fully activated and the PA imaging depth therefore can be guaranteed. Meanwhile, since the wavelength of the PA excitation source is located at the NIR region, the remotely triggerable and controllable external optical stimulus (980 nm) can be flexibly adapted to the PA imaging system.

CONCLUSIONS

In conclusion, we successfully demonstrated the feasibility of W-VO_2@PEG NPs as a PA contrast agent for NIR PA imaging with dynamic-enhanced imaging contrast and imaging depth. The synthesized W-VO_2@PEG NPs exhibited great temperature responsivity close to human-body temperature with high reversibility. The detectable imaging depth at 1064 nm was assessed by identifying the PA signals of W-VO_2@PEG NPs to be 1.5 cm in chicken tissue. The feasibility of clinical application is verified by conducting PA imaging of tumors in mice. These results demonstrate that W-VO_2@PEG NPs can be used as reliable PA agents for dynamic contrast-enhanced PA imaging with improved imaging depth.

METHODS

Preparation of W-VO_2@PEG Nanoprobes. W-VO_2 (20 mg) was dispersed in toluene (2 mL) and further mixed with a solution containing DOPA-PIMA PEG (40 mg) in deionized water (40 mL). The reaction mixture was stirred at room temperature for 6 h. The resulting solution was then sonicated and filtered with a 0.45 μm disposable syringe filter for the removal of larger particles. Finally, a centrifugal filtration device (Millipore, M_w cutoff = 100 kDa) was utilized to remove possible free ligands.

Characterizations. The raw material (W-VO_2 powder) was prepared based on the hydrothermal synthesis method by a chemical synthesis company (Hangzhou Jikang New Materials Co., Ltd.) referred to in a reported work.[57] The authors prepared W-VO_2@PEG NPs in our lab by surface modification with PEG to enhance the water solubility and the biocompatibility of the prepared NPs.

***In Vitro* PA Imaging.** For *in vitro* PA imaging, the scanned samples were two polyethylene transparent hoses filled with W-VO_2@PEG solution and a graphene dispersion of the same concentration, and three polyethylene transparent hoses filled with W-VO_2@PEG NPs of 0.1, 0.2, and 0.3 mg/mL. Then A-scans were performed using a PA imaging system equipped with a laser with an excitation wavelength of 1064 nm, a pulse width of 11 ns, and a repetition rate of 5000 Hz, and the temperature was controlled through a temperature controller.

***In Vivo* PA Imaging.** For *in vivo* PA imaging in the NIR-II window, EMT6 tumor-bearing mice were *in situ* injected with W-VO_2 solution (1.5 mg/kg). After irradiation by a 980 nm CW laser (0.5 W/cm^2) for different times, a B-scan of the section of tumor was performed using a PA imaging system equipped with a laser with an excitation wavelength of 1064 nm. The structural information of the tumor was provided by US images.

Animal and Tumor Model. All animal studies were conducted in accordance with the Guide for the Care and Use of Laboratory Animals (Ministry of Science and Technology of China, 2006). Female Balb/c mice (4−5 weeks) were purchased from the Animal Center of Southern Medical University. EMT6 cells (5×10^6 cells) were subcutaneously injected into the back of the mice, and the mice were raised in an SPF environment. After the tumor volume reached 1200 mm^3, Hypnorm/Midazolam was used to anesthetize the mice, and then the experiment was started.

***In Vitro* Cytotoxicity Assay of W-VO$_2$@PEG NPs.** The EMT6 and 4T1 cells were seeded into 96-well plates and incubated with different concentrations of W-VO$_2$@PEG NPs, for 24 h at 37 °C. The viability of the cells was evaluated using the CCK-8 kit according to the manufacturer's protocol.

ASSOCIATED CONTENT

Supporting Information

The Supporting Information is available free of charge at https://pubs.acs.org/doi/10.1021/acsnano.1c07511.

> Descriptions and details of the experimental methods: characterization of the W-VO$_2$@PEG NPs, the CT response of the W-VO$_2$@PEG NPs, experimental demonstration of the W-doping-enhanced optical absorption of VO$_2$ NPs, phase transition temperature points of W-VO$_2$@PEG NPs and VO$_2$ nanoparticles, photothermal performance of the prepared W-VO$_2$@PEG NPs, temperature stability of the W-VO$_2$@PEG NPs at different depths by using a 980 nm laser with different power, experimental measurement of the phase transition response time for the W-VO$_2$@PEG NPs, *in vitro* demonstration of the photothermal effect enhanced PA effect for the W-VO$_2$@PEG NPs by using a 980 nm laser, photothermal-induced cell killing at different temperatures, metabolism of the W-VO$_2$@PEG NPs (PDF)

AUTHOR INFORMATION

Corresponding Authors

Yujiao Shi − *MOE Key Laboratory of Laser Life Science & Institute of Laser Life Science, College of Biophotonics, South China Normal University, Guangzhou 510631, China; Guangdong Provincial Key Laboratory of Laser Life Science, College of Biophotonics, South China Normal University, Guangzhou 510631, China;* orcid.org/0000-0001-7140-9047; Email: shiyuj@scnu.edu.cn

Da Xing − *MOE Key Laboratory of Laser Life Science & Institute of Laser Life Science, College of Biophotonics, South China Normal University, Guangzhou 510631, China; Guangdong Provincial Key Laboratory of Laser Life Science, College of Biophotonics, South China Normal University, Guangzhou 510631, China;* orcid.org/0000-0001-9752-8458; Email: xingda@scnu.edu.cn

Authors

Liantong Li − *MOE Key Laboratory of Laser Life Science & Institute of Laser Life Science, College of Biophotonics, South China Normal University, Guangzhou 510631, China; Guangdong Provincial Key Laboratory of Laser Life Science, College of Biophotonics, South China Normal University, Guangzhou 510631, China*

Huazhen Chen − *MOE Key Laboratory of Laser Life Science & Institute of Laser Life Science, College of Biophotonics, South China Normal University, Guangzhou 510631, China; Guangdong Provincial Key Laboratory of Laser Life Science, College of Biophotonics, South China Normal University, Guangzhou 510631, China*

Complete contact information is available at:
https://pubs.acs.org/10.1021/acsnano.1c07511

Author Contributions

L.L., H.C., Y.S., and D.X. designed the experiment. L.L. and H.C. contributed to the system construction and performed the sample fabrications. L.L., H.C., and Y.S. performed the experiment and data analysis. Y.S. and D.X. wrote the draft of the manuscript. Y.S. and D.X. supervised the project. L.L., Y.S., H.C., and D.X. were involved in discussions. All authors took part in the discussion and revision and approved the final copy of the manuscript.

Notes

The authors declare no competing financial interest.

ACKNOWLEDGMENTS

Financial support was provided by the National Natural Science Foundation of China (Nos. 61627827, 61805085, 12174125), Guangdong Basic and Applied Basic Research Foundation (2021A1515011874), Science and Technology Planning Project of Guangdong Province, China (Nos. 2015B020233016, 2018A030310519), the Guangzhou Science and Technology Plan Project (No. 201904010321), and the Science and Technology Program of Guangzhou (No. 2019050001).

REFERENCES

(1) Xu, M.; Wang, L. V. Photoacoustic Imaging in Biomedicine. *Rev. Sci. Instrum.* **2006**, *77*, 041101.

(2) Zackrisson, S.; Van De Ven, S.; Gambhir, S. S. Light in and Sound out: Emerging Translational Strategies for Photoacoustic Imaging. *Cancer Res.* **2014**, *74*, 979−1004.

(3) Beard, P. Biomedical Photoacoustic Imaging. *Interface Focus* **2011**, *1*, 602−631.

(4) Mallidi, S.; Luke, G. P.; Emelianov, S. Photoacoustic Imaging in Cancer Detection, Diagnosis, and Treatment Guidance. *Trends Biotechnol.* **2011**, *29*, 213−221.

(5) Cheng, Z.; Ma, H.; Wang, Z.; Yang, S. *In Vivo* Volumetric Monitoring of Revascularization of Traumatized Skin Using Extended Depth-of-Field Photoacoustic Microscopy. *Front. Optoelectron.* **2020**, *13*, 307−317.

(6) Huang, K.; Zhang, Y.; Lin, J.; Huang, P. Nanomaterials for Photoacoustic Imaging in the Second Near-Infrared Window. *Biomater. Sci-UK.* **2019**, *7*, 472−479.

(7) Ge, X.; Fu, Q.; Bai, L.; Chen, B.; Wang, R.; Gao, S.; Song, J. Photoacoustic Imaging and Photothermal Therapy in the Second Near-Infrared Window. *New J. Chem.* **2019**, *43*, 8835−8851.

(8) Jung, D.; Park, S.; Lee, C.; Kim, H. Recent Progress on Near-Infrared Photoacoustic Imaging: Imaging Modality and Organic Semiconducting Agents. *Polymers-Basel* **2019**, *11*, 1693.

(9) Lyu, Y.; Li, J.; Pu, K. Second Near-Infrared Absorbing Agents for Photoacoustic Imaging and Photothermal Therapy. *Small Methods* **2019**, *3*, 1900553.

(10) Upputuri, P. K.; Pramanik, M. Recent Advances in Photoacoustic Contrast Agents for *in Vivo* Imaging. *Wires. Nanomed. Nanobi.* **2020**, *12*, No. e1618.

(11) Fu, Q.; Zhu, R.; Song, J.; Yang, H.; Chen, X. Photoacoustic Imaging: Contrast Agents and Their Biomedical Applications. *Adv. Mater.* **2018**, *31*, 1805875.

(12) Luke, G. P.; Yeager, D.; Emelianov, S. Y. Biomedical Applications of Photoacoustic Imaging with Exogenous Contrast Agents. *Ann. Biomed. Eng.* **2012**, *40*, 422−437.

(13) Weber, J.; Beard, P. C.; Bohndiek, S. E. Contrast Agents for Molecular Photoacoustic Imaging. *Nat. Methods* **2016**, *13*, 639−650.

(14) Wang, Z.; Zhan, M.; Li, W.; Chu, C.; Xing, D.; Lu, S.; Hu, X. Photoacoustic Cavitation-Ignited Reactive Oxygen Species to Amplify Peroxynitrite Burst by Photosensitization-Free Polymeric Nanocapsules. *Angew. Chem., Int. Ed.* **2021**, *60*, 4720−4731.

(15) Zheng, J.; Zeng, Q.; Zhang, R.; Xing, D.; Zhang, T. Dynamic-Reversible Photoacoustic Probe for Continuous Ratiometric Sensing and Imaging of Redox Status *in Vivo*. *J. Am. Chem. Soc.* **2019**, *141*, 19226−19230.

(16) Chen, Y. S.; Zhao, Y.; Yoon, S. J.; Gambhir, S. S.; Emelianov, S. Miniature Gold Nanorods for Photoacoustic Molecular Imaging in the Second Near-Infrared Optical Window. *Nat. Nanotechnol.* **2019**, *14*, 465−472.

(17) Li, J.; Xiao, H.; Yoon, S. J.; Liu, C.; Matsuura, D.; Tai, W.; Song, L.; O'Donnell, M.; Cheng, D.; Gao, X. Functional Photoacoustic Imaging of Gastric Acid Secretion Using pH-Responsive Polyaniline Nanoprobes. *Small* **2016**, *12*, 4690−4696.

(18) Chen, Q.; Liu, X.; Chen, J.; Zeng, J.; Cheng, Z.; Liu, Z. A Self-Assembled Albumin-Based Nanoprobe for *in Vivo* Ratiometric Photoacoustic pH Imaging. *Adv. Mater.* **2015**, *27*, 6820−6827.

(19) Chen, Q.; Liu, X.; Zeng, J.; Cheng, Z.; Liu, Z. Albumin-NIR Dye Self-Assembled Nanoparticles for Photoacoustic pH Imaging and pH-Responsive Photothermal Therapy Effective for Large Tumors. *Biomaterials* **2016**, *98*, 23−30.

(20) Jeevarathinam, A. S.; Lemaster, J. E.; Chen, F.; Zhao, E.; Jokerst, J. V. Photoacoustic Imaging Quantifies Drug Release from Nanocarriers *via* Redox Chemistry of Dye-Labeled Cargo. *Angew. Chem., Int. Ed.* **2020**, *59*, 4678−4683.

(21) Basal, L. A.; Yan, Y.; Shen, Y.; Haacke, E. M.; Mehrmohammadi, M.; Allen, M. J. Oxidation-Responsive, $Eu^{II/III}$-Based, Multimodal Contrast Agent for Magnetic Resonance and Photoacoustic Imaging. *ACS Omega* **2017**, *2*, 800−805.

(22) Ng, K. K.; Shakiba, M.; Huynh, E.; Weersink, R. A.; Roxin, A.; Wilson, B. C.; Zheng, G. Stimuli-Responsive Photoacoustic Nanoswitch for *in Vivo* Sensing Applications. *ACS Nano* **2014**, *8*, 8363−8373.

(23) Meng, Z.; Zhou, X.; She, J.; Zhang, Y.; Feng, L.; Liu, Z. Ultrasound-Responsive Conversion of Microbubbles to Nanoparticles to Enable Background-Free *in Vivo* Photoacoustic Imaging. *Nano Lett.* **2019**, *19*, 8109−8117.

(24) Sivasubramanian, K.; Mathiyazhakan, M.; Wiraja, C.; Upputuri, P. K.; Xu, C.; Pramanik, M. Near-Infrared Light-Responsive Liposomal Contrast Agent for Photoacoustic Imaging and Drug Release Applications. *J. Biomed. Opt.* **2017**, *22*, 041007.

(25) Huang, J.; Pu, K. Activatable Molecular Probes for Second Near-Infrared Fluorescence, Chemiluminescence, and Photoacoustic Imaging. *Angew. Chem.* **2020**, *132*, 11813−11827.

(26) Miao, Q.; Pu, K. Emerging Designs of Activatable Photoacoustic Probes for Molecular Imaging. *Bioconjugate Chem.* **2016**, *27*, 2808−2823.

(27) Wang, X.; Wang, X.; Zhong, X.; Li, G.; Yang, Z.; Gong, Y.; Cheng, L. V-TiO_2 Nanospindles with Regulating Tumor Microenvironment Performance for Enhanced Sonodynamic Cancer Therapy. *Appl. Phys. Rev.* **2020**, *7*, 041411.

(28) Karimi, M.; Sahandi Zangabad, P.; Ghasemi, A.; Amiri, M.; Bahrami, M.; Malekzad, H.; Ghahramanzadeh Asl, H.; Mahdieh, Z.; Bozorgomid, M.; Ghasemi, A.; Rahmani Taji Boyuk, M. R.; Hamblin, M. R. Temperature-Responsive Smart Nanocarriers for Delivery of Therapeutic Agents: Applications and Recent Advances. *ACS Appl. Mater. Interfaces* **2016**, *8*, 21107−21133.

(29) Fan, S. Y.; Hao, Y. N.; Zhang, W. X.; Kapasi, A.; Shu, Y.; Wang, J. H.; Chen, W. Poly (ionic liquid)-Gated $CuCo_2S_4$ for pH/Thermo-Triggered Drug Release and Photoacoustic Imaging. *ACS Appl. Mater. Interfaces* **2020**, *12*, 9000−9007.

(30) Kim, T.; Zhang, Q.; Li, J.; Zhang, L.; Jokerst, J. V. A Gold/Silver Hybrid Nanoparticle for Treatment and Photoacoustic Imaging of Bacterial Infection. *ACS Nano* **2018**, *12*, 5615−5625.

(31) Yang, Z.; Song, J.; Tang, W.; Fan, W.; Dai, Y.; Shen, Z.; Lin, L.; Cheng, S.; Liu, Y.; Niu, G.; Rong, P.; Wang, W.; Chen, X. Stimuli-Responsive Nanotheranostics for Real-Time Monitoring Drug Release by Photoacoustic Imaging. *Theranostics* **2019**, *9*, 526.

(32) Cui, D.; Li, P.; Zhen, X.; Li, J.; Jiang, Y.; Yu, A.; Pu, K. Thermoresponsive Semiconducting Polymer Nanoparticles for Contrast-Enhanced Photoacoustic Imaging. *Adv. Funct. Mater.* **2019**, *29*, 1903461.

(33) Chen, Y. S.; Yoon, S. J.; Frey, W.; Dockery, M.; Emelianov, S. Dynamic Contrast-Enhanced Photoacoustic Imaging Using Photothermal Stimuli-Responsive Composite Nanomodulators. *Nat. Commun.* **2017**, *8*, 15782.

(34) Rizwan, M.; Yahya, R.; Hassan, A.; Yar, M.; Azzahari, A. D.; Selvanathan, V.; Sonsudin, F.; Abouloula, C. N. pH Sensitive Hydrogels in Drug Delivery: Brief History, Properties, Swelling, and Release Mechanism, Material Selection and Applications. *Polymers-Basel* **2017**, *9*, 137.

(35) Samanipour, R.; Wang, T.; Werb, M.; Hassannezhad, H.; Rangel, J. M. L.; Hoorfar, M.; Hasan, A.; Lee, C. K.; Shin, S. R. Ferritin Nanocage Conjugated Hybrid Hydrogel for Tissue Engineering and Drug Delivery Applications. *ACS Biomater. Sci. Eng.* **2020**, *6*, 277−287.

(36) Smith, A. M.; Mancini, M. C.; Nie, S. Second Window for *in Vivo* Imaging. *Nat. Nanotechnol.* **2009**, *4*, 710−711.

(37) Feng, Z.; Tang, T.; Wu, T.; Yu, X.; Zhang, Y.; Wang, M.; Qian, J. Perfecting and Extending the Near-Infrared Imaging Window. *Light-Sci. Appl.* **2021**, *10*, 197.

(38) Field, M.; Hillman, C.; Stupar, P.; Hacker, J.; Lee, K. J. Vanadium Dioxide Phase Change Switches. *Proc. SPIE* **2015**, *9479*, 947908.

(39) Sun, A.; Guo, H.; Gan, Q.; Yang, L.; Liu, Q.; Xi, L. Evaluation of Visible NIR-I and NIR-II Light Penetration for Photoacoustic Imaging in Rat Organs. *Opt. Express* **2020**, *28*, 9002−9013.

(40) Jiang, Y.; Pu, K. Molecular Fluorescence and Photoacoustic Imaging in the Second Near-Infrared Optical Window Using Organic Contrast Agents. *Adv. Biosyst.* **2018**, *2*, 1700262.

(41) Kakiuchida, H.; Jin, P.; Nakao, S.; Tazawa, M. Optical Properties of Vanadium Dioxide Film during Semiconductive-Metallic Phase Transition. *Jpn. J. Appl. Phys.* **2007**, *46*, L113−L116.

(42) Peng, Z.; Wang, Y.; Du, Y.; Lu, D.; Sun, D. Phase Transition and IR Properties of Tungsten-Doped Vanadium Dioxide Nanopowders. *J. Alloy. Compd.* **2009**, *480*, 537−540.

(43) Manning, T. D.; Parkin, I. P.; Pemble, M. E.; Sheel, D.; Vernardou, D. Intelligent Window Coatings: Atmospheric Pressure Chemical Vapor Deposition of Tungsten-Doped Vanadium Dioxide. *Chem. Mater.* **2004**, *16*, 744−749.

(44) Li, M.; Magdassi, S.; Gao, Y.; Long, Y. Hydrothermal Synthesis of VO_2 Polymorphs: Advantages, Challenges and Prospects for the Application of Energy Efficient Smart Windows. *Small* **2017**, *13*, 1701147.

(45) Chen, L.; Huang, C.; Xu, G.; Miao, L.; Shi, J.; Zhou, J.; Xiao, X. Synthesis of Thermochromic W-Doped VO_2 (M/R) Nanopowders by a Simple Solution-Based Process. *J. Nanomater.* **2012**, *2012*, 491051.

(46) Zhang, J.; He, H.; Xie, Y.; Pan, B. Theoretical Study on the Tungsten-Induced Reduction of Transition Temperature and the Degradation of Optical Properties for VO_2. *J. Chem. Phys.* **2013**, *138*, 114705.

(47) Guo, H.; Wang, Y. G.; Fu, H. R.; Jain, A.; Chen, F. G. Influence of Dopant Valence on the Thermochromic Properties of VO_2 Nanoparticles. *Ceram. Int.* **2021**, *47*, 21873−21881.

(48) Chen, L.; Ye, H.; Liu, Y.; Wu, D.; Ma, R.; Yu, Z. Numerical Investigations of an Optical Switch Based on a Silicon Stripe Waveguide Embedded with Vanadium Dioxide Layers. *Photonics Res.* **2017**, *5*, 335−339.

(49) Shao, Z.; Cao, X.; Luo, H.; Jin, P. Recent Progress in the Phase-Transition Mechanism and Modulation of Vanadium Dioxide Materials. *NPG Asia Mater.* **2018**, *10*, 581−605.

(50) Wang, S.; Liu, M.; Kong, L.; Long, Y.; Jiang, X.; Yu, A. Recent Progress in VO_2 Smart Coatings: Strategies to Improve the Thermochromic Properties. *Progress in Mater. Sci.* **2016**, *81*, 1−54.

(51) Liu, K.; Lee, S.; Yang, S.; Delaire, O.; Wu, J. Recent Progresses on Physics and Applications of Vanadium Dioxide. *Mater. Today* **2018**, *21*, 875−896.

(52) Ke, Y.; Wang, S.; Liu, G.; Li, M.; White, T. J.; Long, Y. Vanadium Dioxide: The Multistimuli Responsive Material and Its Applications. *Small* **2018**, *14*, 1802025.

(53) He, X.; Zeng, Y.; Xu, X.; Gu, C.; Chen, F.; Wu, B.; Wang, C.; Xing, H.; Chen, X.; Chu, J. Orbital Change Manipulation Metal-Insulator Transition Temperature in W-Doped VO_2. *Phys. Chem. Chem. Phys.* **2015**, *17*, 11638−11646.

(54) Ling, C.; Zhao, Z.; Hu, X.; Li, J.; Zhao, X.; Wang, Z.; Zhao, Y.; Jin, H. W Doping and Voltage Driven Metal-Insulator Transition in VO_2 Nano-Films for Smart Switching Devices. *ACS Appl. Nano Mater.* **2019**, *2*, 6738−6746.

(55) Lee, W. J.; Chang, Y. H. Growth without Postannealing of Monoclinic VO_2 Thin Film by Atomic Layer Deposition Using VCl_4 as Precursor. *Coatings* **2018**, *8*, 431.

(56) Karaoglan-Bebek, G.; Hoque, M. N. F.; Holtz, M.; Fan, Z.; Bernussi, A. A. Continuous Tuning of W-Doped VO_2 Optical Properties for Terahertz Analog Applications. *Appl. Phys. Lett.* **2014**, *105*, 201902.

(57) Shi, J.; Zhou, S.; You, B.; Wu, L. Preparation and Thermochromic Property of Tungsten-Doped Vanadium Dioxide Particles. *Sol. Energy Mater. Sol. C* **2007**, *91*, 1856−1862.